



**HAL**  
open science

## Prediction of the mechanical response of canine humerus to three-point bending using subject-specific finite element modelling

Cédric P. Laurent, Béatrice Böhme, Marlène Mengoni, Vinciane d'Otreppe, Marc Balligand, Jean-Philippe Ponthot

### ► To cite this version:

Cédric P. Laurent, Béatrice Böhme, Marlène Mengoni, Vinciane d'Otreppe, Marc Balligand, et al.. Prediction of the mechanical response of canine humerus to three-point bending using subject-specific finite element modelling. *Proceedings of the Institution of Mechanical Engineers, Part H: Journal of Engineering in Medicine*, 2016, 230 (7), pp.639 - 649. 10.1177/0954411916644269 . hal-01416475

**HAL Id: hal-01416475**

**<https://hal.univ-lorraine.fr/hal-01416475>**

Submitted on 27 Mar 2019

**HAL** is a multi-disciplinary open access archive for the deposit and dissemination of scientific research documents, whether they are published or not. The documents may come from teaching and research institutions in France or abroad, or from public or private research centers.

L'archive ouverte pluridisciplinaire **HAL**, est destinée au dépôt et à la diffusion de documents scientifiques de niveau recherche, publiés ou non, émanant des établissements d'enseignement et de recherche français ou étrangers, des laboratoires publics ou privés.

## Prediction of the mechanical response of canine humerus to three-point bending using subject-specific finite element modelling

Cédric P. Laurent<sup>1,2</sup>, Béatrice Böhme<sup>3</sup>, Marlène Mengoni<sup>1,4</sup>, Vinciane d'Otreppe<sup>1</sup>, Marc Balligand<sup>3</sup>, Jean-Philippe Ponthot<sup>1</sup>

1 University of Liege, Department of Aerospace and Mechanical Engineering, Belgium

2 CNRS, LEMTA, UMR 7563, Université de Lorraine, France

3 University of Liege, Department of Clinical Sciences, College of Veterinary Medicine, Belgium

4 Institute of Medical and Biological Engineering, School of Mechanical Engineering, University of Leeds, UK

Corresponding author:

Cédric P. Laurent, CNRS, LEMTA, UMR 7563, Université de Lorraine, 2 avenue de la forêt de Haye, F-54502 Vandoeuvre-lès-Nancy, France

Email: [Cedric.laurent@univ-lorraine.fr](mailto:Cedric.laurent@univ-lorraine.fr)

Submitted as an original article

Word count: 3874 (max 5000)

## **Abstract**

Subject-specific finite element (FE) models could improve decision making in canine long bone fracture repair. However, it preliminary requires that FE models predicting the mechanical response of canine long bone are proposed and validated. We present here a combined experimental-numerical approach to test the ability of subject-specific FE models to predict the bending response of seven pairs of canine humeri directly from medical images. Our results show that bending stiffness and yield load are predicted with a mean absolute error of 10.1% ( $\pm 5.2\%$ ) for the fourteen samples. This study constitutes a basis for the forthcoming optimization of canine long bone fracture repair.

## **Keywords**

Finite element modelling

Subject-specific

Canine bone material properties

Bending test

Canine humerus

## 1 Introduction

2 Long bone fracture constitutes a common reason for medical consultation within  
3 veterinary orthopaedic services<sup>1,2</sup>, as emphasized by the substantial recent literature  
4 concerning the choice of adapted implants<sup>3-6</sup>. Associated surgical interventions are  
5 often complex given that each fracture has its own particularities. Canine bone fracture  
6 repair differs from the human case in the sense that (1) the physiological characteristics  
7 and morphology of the injured bones in animals vary considerably<sup>7</sup>, (2) the animal is not  
8 able to limit its activity during the post-operative period, which may lead to premature  
9 overloading, and (3) the surgeon is often confronted to cost limitations concerning  
10 orthopaedic material. As a result, the treatment of such fractures (implant type,  
11 dimension, location ...) depends to some extent on the surgeon's experience, who tries  
12 to find a trade-off between a minimum stiffness required for fracture stabilization and  
13 a sufficient flexibility essential for bone remodelling. Although available handbooks  
14 guide the surgeon in the choice of a suited treatment for each particular fracture, they  
15 are still based on empirical knowledge, and there is a lack of studies assessing the effect  
16 of different treatment types on the biomechanical properties of the reconstructed bone.  
17 This insufficient knowledge may partly explain the complications that are still frequent  
18 in the field of canine fracture repair<sup>8,9</sup>.

19 In order to improve the surgical procedure, ex-vivo experiments<sup>10,11</sup> as well as numerical  
20 biomechanical studies<sup>12-14</sup> have been reported. Indeed, numerical approaches, such as  
21 Finite Element (FE) modelling may enable to evaluate non-invasively the effect of  
22 various implants or their combination on the same bone sample. However, these FE  
23 studies are often based on simplistic bone models (i.e. elastic, linear, homogeneous  
24 cortical and trabecular tissues, etc...). A milestone in delivering relevant data in a  
25 subject-specific approach consists of including the bone external geometry and  
26 heterogeneous material properties from the information available in CT images. Such  
27 subject-specific FE approaches have been developed in human long bone analysis and  
28 satisfyingly predicted the failure risk in proximal femur<sup>15-18</sup>. However, available studies  
29 in human have often led to moderately accurate results as far as the prediction of the  
30 global biomechanical response of long bones are concerned, probably due to  
31 accumulating inherent approximations throughout the model generation. Particularly,  
32 it is not clear if the consideration of density-dependent material properties leads to  
33 better results than the modelling of long bone with two materials (trabecular and  
34 cortical tissues) separated from a density criterion. The interest of considering  
35 anisotropic material properties is also not clear. Moreover, if one wants to extend these  
36 subject-specific FE models to canine bone, a supplementary difficulty will come from the  
37 variability of bone material properties from one breed to another<sup>19</sup>, and from the

38 absence of data concerning relationships between CT information and bone material  
39 properties for dogs.

40 Such FE models are usually validated using *ex vivo* mechanical tests such as bending<sup>20,21</sup>,  
41 torsion<sup>22</sup> or compression<sup>17,23</sup>. These combined experimental-numerical approaches  
42 require that a particular attention is paid to the application of similar Boundary  
43 Conditions (BC), such as load application and displacement restriction, in the  
44 experimental and computational setups<sup>24</sup>.

45 In the present contribution, the hypothesis was that subject-specific FE models are able  
46 to predict the global mechanical response of canine long bones to three-point bending  
47 tests. The aims of the present work were therefore (1) to provide a direct subject-  
48 specific validation of canine long bone FE models including a novel density-elasticity law;  
49 and (2) to assess the requirements for the bone material model to replicate measured  
50 *ex vivo* behaviour.

## 51 **Material and Methods**

52 A combined experimental and computational approach was developed to validate the  
53 FE models with *ex vivo* three-point bending data, i.e. overall load/deflection behaviour  
54 and local fracture patterns. All dynamic FE analyses were performed using the in house  
55 non-linear implicit FE code MetaFor (metafor.ltas.ulg.ac.be).

56 *Specimen preparation, imaging, and mechanical testing*

57 Eight pairs of canine humeri were initially harvested from adult dogs euthanized for  
58 reasons unrelated to this study. After harvesting, one dog (i.e. one pair of humeri) was  
59 excluded from this study due to the observation of severe knee arthrosis. Dog weights  
60 finally ranged from 19 to 39kg. Soft tissues were carefully removed and samples were  
61 wrapped in saline soaked sponges and stored at -20°C. Samples were prepared for  
62 three-point bending mechanical tests at room temperature. In order to accurately  
63 control the location of the bones within the custom bending stand and to restrict  
64 rotations around the bone diaphysis axis during the bending tests, the epiphyses were  
65 embedded into 60×60×60mm<sup>3</sup> moulds made of two-component polymeric resin  
66 (Motip®, Germany) (Figure 1). A particular attention was paid to define resin moulds  
67 orientation with respect to the bone sample position in a reproducible way. Firstly, we  
68 used the origin of the medial and lateral collateral ligaments as anatomical landmarks  
69 to define a reference axis. Then, the distal resin mould was created in such a way that  
70 this anatomical reference axis was parallel to two surfaces of the resin block (namely its  
71 cranio-caudal and proximal-distal surfaces). The second mould was perfectly aligned  
72 with the first one, using custom-made jig (Figure 1.a).

73 The samples were imaged using a CT-scanner (Siemens SOMATOM at 120 kVp) with a  
74 slice thickness of 0.75mm and a spatial resolution of 0.1445mm. A phantom (Siemens

75 BMD calibration phantom<sup>25</sup>) was used to calibrate the bone densities with respect to  
76 the Hounsfield Units (HU) issued from the CT acquisition<sup>18,26</sup>. Particular attention was  
77 paid to keep the samples packed in saline-soaked wraps throughout the procedure in  
78 order to avoid tissue dehydration. The following relation was obtained:

79 
$$\rho = 4.9332 \cdot 10^{-4} HU + 0.9839 (1)$$

80 Samples were placed on a custom adjustable bending stand (Figure 1.b) made of two  
81 steel half-cylinders. The cylinders positions were adjusted so that they were in contact  
82 with the middle of each resin mould in the axial direction of the bone. The bending tool  
83 consisted in a cylindrical punch located longitudinally at half the distance between the  
84 two resin moulds. The stand was mounted in a 100 kN servo-hydraulic testing machine  
85 (Zwick/Roell, Ulm, Germany, load cell : XForce HP 5 kN). A medial-lateral displacement  
86 was applied to the bending tool at a speed of 0.2 mm.s<sup>-1</sup> after a preload of 50 N. The  
87 samples were tested until complete fracture. Tool displacement (hereafter called  
88 deflection) and vertical force (i.e. shear force) were recorded. Two high speed cameras  
89 (Vision Research v7.3) recording 1000 frames/s were used in order to visualize the  
90 fracture onset.



91 *Finite Element modelling*

92 Each tested sample was modelled with a subject-specific approach. The geometry of the  
93 bone were built from the 3D CT data using 3D-Slicer<sup>27</sup> ([www.slicer.org](http://www.slicer.org)) for segmentation  
94 and a dedicated in-house algorithm<sup>28</sup> for the generation of smooth multi-region surface  
95 meshes. The bone volume mesh was obtained using Tetgen (WIAS, Berlin, Germany),  
96 generating linear tetrahedra. Final mesh size was issued from a mesh dependency  
97 analysis reported hereafter.

98 The resin moulds were not meshed in the FE model but considered as single deformable  
99 hexahedrons whose coordinates were automatically computed from the boundaries of  
100 resin moulds in the surface mesh (Figure 1.b). Resin was considered linear elastic, with  
101 an elastic modulus of 900 MPa characterized from preliminary experiments. Elements  
102 were assigned a density issued from the calibration phantom, and equal to  $1\text{g}\cdot\text{cm}^{-3}$  for  
103 resin. The interaction between the bone and the resin moulds was modelled using  
104 springs (arbitrary stiffness of  $100\text{ N mm}^{-1}$ ) linking the hexahedron nodes with each of  
105 the bone surface nodes located within the resin moulds (Figure 1.b) in order to constrain  
106 the relative displacement between bone and resin. This numerical representation of the  
107 resin blocks is totally equivalent to a penalty formulation in contact algorithms with  
108 bilateral restrictions to enforce the continuity of the displacement field at the interface

109 between bone and resin. The proximal resin mould was restrained in the cranio-caudal  
110 direction.

111 The bending stand was modelled as two rigid half-cylinders located longitudinally at the  
112 middle of each resin moulds. The frictional contact condition between the resin moulds  
113 and the bending stand was modelled with a Coulomb's law, with static and dynamic  
114 friction coefficients set at 0.7, corresponding to a dry static contact between steel and  
115 steel<sup>29</sup>. This value was chosen due to the lack of published value for resin-steel contact.  
116 Each half-cylinders of the bending stand were restrained in their 6 degrees of freedom.

117 The bending tool was modelled as a rigid half-cylinder located, as marked  
118 experimentally, at half the distance between the two resin moulds. Displacement was  
119 applied to the tool in the medial-lateral direction. Contact between the bending tool and  
120 the bone surface was modelled as sticking contact.

121 A sensitivity analysis was performed analysing the effect of the resin properties, the  
122 stiffness of the springs used to attach bone to resin blocks and the friction coefficient  
123 between resin and stand on the predicted bone stiffness and yield load. Load-deflection  
124 curves were obtained as the sum of the medial-lateral component of the contact force  
125 and the tool displacement at each time step. The experimental preload was mimicked  
126 by excluding the initial forces below 50N from the simulation results.

127 For each sample, user interaction was only needed for the image segmentation step. To  
128 avoid user variation, all other steps of the model creation and analysis were automated,  
129 based on the size of the samples extracted from the segmented data. All FE analyses  
130 were performed using local HPC facilities (parallel computation on 144 cores).

### 131 *Bone material models*

132 Three different materials models were considered for the bone: a density-dependent  
133 transversely isotropic model, a density-dependent isotropic model, and a two-material  
134 isotropic model (one material model for cortical bone and one for trabecular bone).

135 For the density dependent models, material parameters were mapped against the HU  
136 values from the CT scans starting from equation (1). The following mapping procedure  
137 was applied: (1) for each mesh element, the smallest rectangular box that embraced the  
138 tetrahedron was defined, (2) for each voxel included within this box, material properties  
139 (see next section) were computed from the density computed from the HU field, and (3)  
140 material properties were averaged on this box and assigned to the mesh element. A  
141 particular attention was paid to reduce the partial volume artefacts: to this end, we  
142 firstly separated the mesh elements that had at least one point belonging to the bone  
143 surface (*outer cells*) from the other mesh elements (*inner cells*). Each outer cell was then  
144 associated to its closest inner cell, and was assigned the HU value of its associated inner

145 cell when it was higher than its own HU value. This procedure significantly reduced the  
146 partial volume artefact, provided that the bone cortical wall was described by a  
147 sufficient number of mesh elements, i.e. that the mesh was sufficiently dense.

148 It is known that the properties of canine bone depends on dog mass<sup>19</sup>. Therefore a  
149 density-elasticity relationship had to be derived for canine bone. It would indeed not be  
150 justified to use a unique density-elasticity relationship determined from human bone.  
151 Published experimental data<sup>19</sup> reported the elastic moduli of canine cortical bone as a  
152 function of dog breed: 13.3GPa (dog mass=5kg), 14.9GPa (dog mass=12kg), 16GPa (dog  
153 mass=25kg), 16.3GPa (dog mass=50kg). Comparing that data to an average reported  
154 elastic modulus of 17.9GPa for human cortical bone<sup>30</sup>, the following relation between  
155 human data and canine data was extrapolated (using a common mean-square method):

$$156 \quad E_{\text{canine}}(\rho) = E_{\text{human}}(\rho) \times (0.3 \exp(-5/m) + 0.64) \quad (2)$$

157 by denoting  $m$  the dog mass. This relation is illustrated on Figure 2, and assumes that  
158 bone properties depend only on dog mass and not on the breed.

159 This canine-to-human relation was used to weight existing density-elasticity  
160 relationships validated for human data:

161 For the density-dependent transversely isotropic model, bone was considered as an  
162 elastoplastic material without distinction between cortical and trabecular tissues

163 (except for density). The elastic part of the model was built from relation (2) and using  
164 an orthotropic elasticity-density relationship for human bone in tension<sup>31</sup>:

$$\begin{aligned} E_l &= 2065\rho^{3.09} & G_{lt} &= 0.29E_l \\ E_t &= 2314\rho^{1.57} & G_{tt} &= 0.2E_l \end{aligned} \quad (3)$$

166 by denoting  $E_l$  and  $E_t$  the elastic moduli (MPa) in the longitudinal and transverse  
167 directions,  $G_{lt}$  and  $G_{tt}$  the shear moduli (MPa), and  $\rho$  ( $\text{g cm}^{-3}$ ) the apparent density issued  
168 from CT calibration. These relations valid for human bone were weighted using relation  
169 (2) in order to model canine bone. Asymmetric elastic material properties were assumed  
170 by considering that the elastic modulus was 6% higher in compression than in tension<sup>32</sup>.

171 The global longitudinal direction was automatically computed for each sample, based  
172 only on the central third of the bone (representing the diaphysis, see Figure 3). The mesh  
173 nodes belonging to the bone surface and included in this part were selected, and used  
174 to compute a least-square line defined as the longitudinal direction. The transverse  
175 direction was defined perpendicularly to this direction, in a plane containing the tool  
176 displacement vector.

177 The yield surface was defined through a Von Mises criterion with linear isotropic  
178 hardening. The initial yield stress was obtained from the yield strain of 0.73% reported

179 for human cortical bone<sup>33</sup> and the mean elastic modulus (defined as the average of  
180 longitudinal and transverse moduli) following the relation:

$$181 \quad \sigma_y = 0.0073(E_l + E_t) / 2 \quad (4)$$

182 The role of the longitudinal stress was therefore considered predominant in the bone  
183 yield. Post-yield hardening was set as 5% of the initial, density-dependent, mean elastic  
184 moduli<sup>34</sup>.

185 The same procedure was applied for the density-dependent isotropic model. The unique  
186 Young modulus was defined as the mean of the computed longitudinal and transverse  
187 modulus for a given bone density (relation (3)) weighted by the correction coefficients  
188 given in relation (2). Yield was modelled identically to the previous model.

189 For the two-material isotropic model, trabecular and cortical canine tissues were  
190 respectively modelled with Young's modulus of 750MPa and 15GPa and a Poisson's ratio  
191 of 0.3<sup>35</sup>. Cortical and trabecular tissues were separated using a threshold in terms of HU  
192 values. Cortical tissue was assumed for HU values superior to either 600HU or 400HU in  
193 order to assess the sensitivity to this parameter. Yield was modelled identically to the  
194 previous models.

195 *Statistical analysis*

196 For each tested bone, bending stiffness (least-square linear regression of the linear part  
197 of force-deflection curve passing through the origin) and yield load (intersection  
198 between a parallel to this linear regression with a 0.1 mm offset and the force-deflection  
199 curve) were extracted and compared between the experimental and computational  
200 data.

201 In order to emphasize the statistical significance of our model, we performed various  
202 statistical analyses from our experimental results (14 samples from 7 dogs) and our  
203 numerical results (56 models: 14 density-dependant transversely isotropic models, 14  
204 density-dependant isotropic models, and 14 two-materials isotropic models with a  
205 segmentation threshold of 400 HU or 600 HU). Analysis of variance (ANOVA) was used  
206 as the common test to quantify the difference between two sets of data, with a default  
207 p-value of 0.01 (when not detailed).

208 **Results**

209 *Experimental results*

210 Experimental results for the seven pairs of humeri are represented in Figure 4. A large  
211 intra- and inter-variability was observed: as an example, a mean difference of 14.6% in  
212 stiffness between the left and right humerus of the same dog. Left and right humerus of

213 the same dog were however not different (both in terms of stiffness and yield load) in  
214 the sense of an ANOVA analysis. The coefficient of variation (ratio between standard  
215 deviation and mean) of the stiffness is equal to 20.2%. The data showed a weak  
216 correlation between dog mass and mean humerus stiffness (correlation coefficient of  
217 0.65). While the failure was sudden for six samples, it was more progressive for the  
218 others and no clear fracture pattern was therefore visible.

#### 219 *Computational results*

220 The meshes resulting from the reconstruction of the segmented CT images together  
221 with the mapping procedure are represented in Figure 5 for all bone samples. Bone  
222 mesh made of approximately 300 000 tetrahedral linear elements (60 000 nodes) led to  
223 a relative difference of 2.5% on strain energy density (SED) and 1.4% on stiffness  
224 compared to the values obtained for 160 000 nodes. The results of the sensitivity study  
225 for one humerus are reported in Table 1. These data emphasize that the simulation  
226 results are not sensitive to resin properties, indicating that the resin does not deform  
227 substantially during the bending test. Moreover, the simulation results are very slightly  
228 sensitive to the stiffness of springs used to attach bone to resin (2% of deviation for a  
229 variation of five orders of magnitude). A stiffness of 100N/mm (i.e. of the same order of  
230 magnitude than the bone bending stiffness) has been consequently selected for every  
231 simulations. However, this sensitivity study emphasizes that the friction coefficient does



232 have an effect on predicted stiffness and yield load. A friction coefficient of 0.7 has been  
233 chosen for the simulations due to the lack of existing data, as long as such data are  
234 difficult to measure experimentally.

235 For the density-dependent transversely isotropic model on the fourteen samples, the  
236 bending stiffness was predicted with a maximum error of 21.7% (absolute value of the  
237 mean error =  $10.1\% \pm 5.2\%$ ). The yield load was predicted with an absolute value of the  
238 mean error  $11\% \pm 11.3\%$ , but was unsatisfyingly predicted for one sample over the  
239 fourteen samples (maximum error = 43.5%, see Figure 6). Correlation coefficients  
240 between predicted and measured values were 0.86 for stiffness and 0.74 for yield load.  
241 A Bland-Altman representation of the simulation results obtained with this model has  
242 also been provided (Figure 7) : it clearly illustrates the good prediction ability of this  
243 model. However, this representation clearly emphasizes that the values of bending  
244 stiffness and yield load are badly predicted for one sample (#6 right).

245 Results of the different models were confronted to experimental results in the sense of  
246 ANOVA statistical tests, and the *p-values* issued from these tests are gathered in Table  
247 2, under the null hypothesis that experimental and simulations results have the same  
248 mean (i.e. if the *p-value* is near to zero, experimental and simulation results are  
249 significantly different). From this analysis, it is clear that the density-dependant  
250 transversely isotropic model is the most predictive model among the four different

251 models tested, and especially compared to the density-dependant isotropic model, as  
252 illustrated on Figure 8. Surprisingly, the computational results are better in the case of  
253 the two-material isotropic models (no matter the segmentation threshold) than in the  
254 case of density-dependant isotropic models.

255 Results of the FE simulations for the two-material isotropic model are represented in  
256 Figure 9, with trabecular and cortical tissues being separated either from HU values of  
257 400 or 600HU in order to quantify the sensitivity of the bending response to this  
258 threshold. There is no statistical difference between the two threshold values used to  
259 separate cortical from trabecular tissue in the case of two-material models.

## 260 **Discussion**

### 261 *Model accuracy*

262 A finite element mesh of 60 000 nodes showed to be a converged mesh for the bone  
263 stiffness and strain energy density (SED). A satisfying prediction of bone stiffness was  
264 obtained for every samples, whereas the yield load was satisfyingly predicted for 13 over  
265 14 samples. The reported computational results were insensitive to the properties  
266 assigned to the resin block holding the bone epiphysis; this indicates that resin blocks  
267 do not deform much during the simulations. The computational representation of those

268 blocks is thus a good approximation of the blocks behaviour and interaction with the  
269 bone.

270 Using the verified and validated non-linear FE software Metafor<sup>36-39</sup> to analyse long  
271 bone three-point bending tests permits high automation of the model pre- and post-  
272 processing steps. This reduces user-variability to the image segmentation step only. All  
273 other parameters, especially as far as the definition of model boundary conditions  
274 representative of the experimental conditions is concerned, are subject only to the  
275 experimental variability.

276 Density-elasticity relationships for canine long bone as a function of dog mass were  
277 determined by weighting human relationships from published canine bone properties.  
278 Using material parameters from literature only, and not specifically calibrated on the  
279 experimental results, the produced models were able to satisfyingly predict bending  
280 stiffness and yield load. However, more detailed studies on microstructure or  
281 composition of canine bone as a function of mass (or breed) would be required in order  
282 to propose a more comprehensive relation.

283 The predictive power of the models for stiffness values and yield loads is here reflected  
284 not only by a good correlation but also by a good concordance, which is less often the  
285 case in published models<sup>40,41</sup>. This therefore suggested that the approach used in this

286 work produces valid models to predict bone stiffness and yield loads in three-point  
287 bending of canine long bones.

### 288 *Comparison between models*

289 The benefit of the non-linear density-dependent transversely isotropic model compared  
290 to the two other models is demonstrated in terms of its improved prediction capability.  
291 However, it is surprising that the two-material isotropic model leads to better  
292 predictions than the density-dependent isotropic model. This may be explained by the  
293 fact that, during a bending test, the bone is essentially subject to tension and  
294 compression, and therefore the longitudinal modulus of the bone plays a crucial role  
295 compared to transverse modulus. In the case of the density-dependant isotropic model,  
296 the computed average Young modulus is therefore underestimated, for a loading  
297 involving mainly the longitudinal direction. Predicted stiffness is thus globally  
298 underestimated using the density-dependant isotropic model. On the contrary, the two-  
299 material model may widely overestimate the Young modulus by considering constant  
300 density for cortical bone, as it is clearly seen that it is not uniform over the cortical bone  
301 (Figure 5). Therefore, , it may lead to higher errors in more complex loading modes even  
302 without involving a huge overestimation of bone properties in the case of bending loads.  
303 For instance, a HU value of 1500HU for cortical bone corresponds to longitudinal and  
304 transverse moduli of 9.7GPa and 4.7GPa respectively using the density-dependant

305 transversely isotropic model, whereas it corresponds to a Young modulus equal to  
306 7.2GPa using the density-dependant isotropic model, and equal to 15GPa in the case of  
307 the two-material models. One other limitation of the two-material model is the  
308 sensitivity of the results to the threshold value chosen to separate trabecular and  
309 cortical tissues, which may be user-dependent. This limit obviously disappears when the  
310 density-dependent model is used.

311 As far as the ease of implementation is concerned, computation times were equivalent  
312 for the three models. However, density-dependant models require to develop and  
313 algorithm in order to link HU values to elastic properties, and also require a calibration  
314 of the CT-scan. Moreover, using a transversely isotropic model requires the definition of  
315 orthotropic axis, which has been approximated in our case for bending tests. More  
316 complex algorithms would be required to assign local orthotropic axis for more complex  
317 loadings. Except for these pre-processing steps, the calculation of the three types of  
318 models is then straightforward.

### 319 *Limitations and challenges*

320 One of the limitation of bending tests lies in the fact that results depend on the friction  
321 coefficient between sample and the bending tools, as illustrated by our sensitivity  
322 analysis and by other authors <sup>42</sup>. Bending stand–resin interaction was modelled with

323 friction coefficient of 0.7 due to the lack of existing values. Even if this friction coefficient  
324 is realistic for such a soft resin, experiments could be performed in order to confirm  
325 these results. However, such measurements are complex to perform, as long as  
326 apparent friction coefficients may be affected by local deformation of the resin due to  
327 the cylindrical shape of the bending stand and the high loads involved. These local  
328 effects are not taken into account in the simulations, as long as resin blocks have been  
329 modelled by a single element. This particular point may be subject to further analyses,  
330 for instance using an inverse approach from similar bending tests on well-known  
331 materials.

332 A simple elastoplastic law with isotropic linear hardening was used as proposed in the  
333 literature<sup>33</sup>, and associated with a Von Mises yield criterion. Even though the use of such  
334 a criterion has been questioned<sup>43</sup>, no consensus has been clearly found and this criterion  
335 is still widely used<sup>34,38,40</sup>. The simulated post-yield response did not reproduce the  
336 plateau observed experimentally for some samples: it may be therefore concluded that  
337 the linear hardening set as 5% of the initial mean modulus as proposed in the literature  
338 was excessive and should be age and breed dependent, or that a perfectly plastic  
339 behaviour might be more representative. Including progressive damage in the model  
340 may lead to better results as the physical phenomenon leading to bone non-linear  
341 behaviour is most probably related to damage rather than plasticity<sup>21,34,38,44</sup>.

342 No distinction was made between cortical and trabecular tissues in the bone material  
343 properties characterising the non-linear behaviour, although the microstructures of  
344 these tissues are clearly different. It is likely that here the trabecular tissue do not  
345 participate substantially to the bone bending response. The material axes were defined  
346 from the mid-line of the diaphysis, as commonly reported in the literature<sup>45,46</sup>, leading  
347 to a global definition of the longitudinal direction. As the segment of interest involved  
348 in the bending test was restricted to the bone diaphysis in which the main orthotropic  
349 direction does not substantially vary, it is unlikely that this simplification has an effect  
350 on the reported results. These two limitations suggest that the validity of the procedure  
351 proposed here is thus probably restricted to the bending mode of deformation.

## 352 **Acknowledgements**

353 The authors would like to acknowledge the Research Council of the University of Liège  
354 for having selected this research in their funding program.

## 355 **Conflicts of interest**

356 There is no conflict of interest in this study.

357 **References**

- 358 1. Kumar, K. *et al.* Occurrence and Pattern of Long Bone Fractures in Growing Dogs  
359 with Normal and Osteopenic Bones. *J. Vet. Med. Ser. A* **54**, 484–490 (2007).
- 360 2. Miller, C. W., Sumner-Smith, G., Sheridan, C. & Pennock, P. W. Using the Unger  
361 system to classify 386 long bone fractures in dogs. *J. Small Anim. Pract.* **39**, 390–393  
362 (1998).
- 363 3. Voss, K., Kull, M. A., Hässig, M. & Montavon, P. M. Repair of long-bone fractures in  
364 cats and small dogs with the Unilock mandible locking plate system. *Vet. Comp.*  
365 *Orthop. Traumatol.* **5**, 398–405 (2009).
- 366 4. Ayyappan, S., Shafiuzama, M., Ganesh, T. N., Das, B. C. & Kumar, R. . A clinical study  
367 on external fixators for long bone fracture management in dogs. *Indian J. Vet. Surg.*  
368 **30**, 90–92 (2009).
- 369 5. Rahal, C., Otoni, C., Pereira, O., Blum, A. & Vulcano, L. Synthesis Pengo System plates  
370 for the treatment of long-bone diaphyseal fractures in dogs. *Vet. Comp. Orthop.*  
371 *Traumatol. VCOT* **21**, 59–63 (2008).
- 372 6. Dueland, R., Johnson, K., Roe, S., Engen, M. & Lesser, A. Interlocking nail treatment  
373 of diaphyseal long-bone fractures in dogs. *J. Am. Vet. Med. Assoc.* **214**, 59–66 (1999).



- 374 7. Palierne, S., Asimus, E., Mathon, D., Meynaud-Collard, P. & Autefage, A. Geometric  
375 analysis of the proximal femur in a diverse sample of dogs. *Res. Vet. Sci.* **80**, 243–  
376 252 (2006).
- 377 8. Dvořák, M., Nečas, A. & Zatloukal, J. Complications of Long Bone Fracture Healing in  
378 Dogs: Functional and Radiological Criteria for their Assessment. *Acta Vet. Brno* **69**,  
379 107–114 (2000).
- 380 9. Jackson, L. C. & Pacchiana, P. D. Common complications of fracture repair. *Clin. Tech.*  
381 *Small Anim. Pract.* **19**, 168–179 (2004).
- 382 10. Blake, C. A. *et al.* Single cycle to failure in bending of three standard and five locking  
383 plates and plate constructs. *Vet. Comp. Orthop. Traumatol. VCOT* **24**, 408–417  
384 (2011).
- 385 11. Zahn, K. *et al.* Mechanical properties of 18 different AO bone plates and the clamp-  
386 rod internal fixation system tested on a gap model construct. *Vet. Comp. Orthop.*  
387 *Traumatol.* **21**, 185–194 (2008).
- 388 12. Nassiri, M., MacDonald, B. & O’Byrne, J. M. Locking compression plate breakage and  
389 fracture non-union: a finite element study of three patient-specific cases. *Eur. J.*  
390 *Orthop. Surg. Traumatol.* **22**, 275–281 (2012).
- 391 13. Oh, J.-K. *et al.* Effect of fracture gap on stability of compression plate fixation: A finite  
392 element study. *J. Orthop. Res.* **28**, 462–467 (2010).

- 393 14. Vajgel, A. *et al.* Comparative Finite Element Analysis of the Biomechanical Stability  
394 of 2.0 Fixation Plates in Atrophic Mandibular Fractures. *J. Oral Maxillofac. Surg.* **71**,  
395 335–342 (2013).
- 396 15. Bessho, M. *et al.* Prediction of proximal femur strength using a CT-based nonlinear  
397 finite element method: Differences in predicted fracture load and site with changing  
398 load and boundary conditions. *Bone* **45**, 226–231 (2009).
- 399 16. Hambli, R., Bettamer, A. & Allaoui, S. Finite element prediction of proximal femur  
400 fracture pattern based on orthotropic behaviour law coupled to quasi-brittle  
401 damage. *Med. Eng. Phys.* **34**, 202–210 (2012).
- 402 17. Tsouknidas, A., Anagnostidis, K., Maliaris, G. & Michailidis, N. Fracture risk in the  
403 femoral hip region: A finite element analysis supported experimental approach. *J.*  
404 *Biomech.* **45**, 1959–1964 (2012).
- 405 18. Hambli, R. & Allaoui, S. A Robust 3D Finite Element Simulation of Human Proximal  
406 Femur Progressive Fracture Under Stance Load with Experimental Validation. *Ann.*  
407 *Biomed. Eng.* **41**, 2515–2527 (2013).
- 408 19. Autefage, A., Paliarne, S., Charron, C. & Swider, P. Effective mechanical properties  
409 of diaphyseal cortical bone in the canine femur. *Vet. J.* **194**, 202–209 (2012).
- 410 20. Duprey, S., Bruyere, K. & Verriest, J.-P. Experimental and simulated flexion tests of  
411 humerus. *Int. J. Crashworthiness* **12**, 153–158 (2007).

- 412 21. Hambli, R. & Thurner, P. J. Finite element prediction with experimental validation of  
413 damage distribution in single trabeculae during three-point bending tests. *J. Mech.*  
414 *Behav. Biomed. Mater.* **27**, 94–106 (2013).
- 415 22. Varghese, B., Short, D., Penmetsa, R., Goswami, T. & Hangartner, T. Computed-  
416 tomography-based finite-element models of long bones can accurately capture  
417 strain response to bending and torsion. *J. Biomech.* **44**, 1374–1379 (2011).
- 418 23. Trabelsi, N., Yosibash, Z., Wutte, C., Augat, P. & Eberle, S. Patient-specific finite  
419 element analysis of the human femur: a double-blinded biomechanical validation. *J.*  
420 *Biomech.* **44**, 1666–1672 (2011).
- 421 24. Viceconti, M., Olsen, S., Nolte, L.-P. & Burton, K. Extracting clinically relevant data  
422 from finite element simulations. *Clin. Biomech. Bristol Avon* **20**, 451–454 (2005).
- 423 25. Kalender, W. A. & Suess, C. A new calibration phantom for quantitative computed  
424 tomography. *Med. Phys.* **14**, 863–866 (1987).
- 425 26. Austman, R. L., Milner, J. S., Holdsworth, D. W. & Dunning, C. E. The effect of the  
426 density–modulus relationship selected to apply material properties in a finite  
427 element model of long bone. *J. Biomech.* **41**, 3171–3176 (2008).
- 428 27. Fedorov, A. *et al.* 3D Slicer as an image computing platform for the Quantitative  
429 Imaging Network. *Magn. Reson. Imaging* **30**, 1323–1341 (2012).

- 430 28. d’Otreppe, V., Boman, R. & Ponthot, J.-P. Generating smooth surface meshes from  
431 multi-region medical images. *Int. J. Numer. Methods Biomed. Eng.* **28**, 642–660  
432 (2012).
- 433 29. Sullivan, J. F. in *Technical Physics* (Wiley, 1988).
- 434 30. Reilly, D. T. & Burstein, A. H. The elastic and ultimate properties of compact bone  
435 tissue. *J. Biomech.* **8**, 393–405 (1975).
- 436 31. Wirtz, D. C. *et al.* Critical evaluation of known bone material properties to realize  
437 anisotropic FE-simulation of the proximal femur. *J. Biomech.* **33**, 1325–1330 (2000).
- 438 32. Li, S., Demirci, E. & Silberschmidt, V. V. Variability and anisotropy of mechanical  
439 behavior of cortical bone in tension and compression. *J. Mech. Behav. Biomed.*  
440 *Mater.* **21**, 109–120 (2013).
- 441 33. Bayraktar, H. H. *et al.* Comparison of the elastic and yield properties of human  
442 femoral trabecular and cortical bone tissue. *J. Biomech.* **37**, 27–35 (2004).
- 443 34. Verhulp, E., van Rietbergen, B. & Huiskes, R. Load distribution in the healthy and  
444 osteoporotic human proximal femur during a fall to the side. *Bone* **42**, 30–35 (2008).
- 445 35. Verim, O., Tasgetiren, S., Er, M. S., Ozdemir, V. & Yuran, A. F. Anatomical evaluation  
446 and stress distribution of intact canine femur. *Int. J. Med. Robot.* **9**, 103–108 (2013).
- 447 36. Boman, R. & Ponthot, J.-P. Efficient ALE mesh management for 3D quasi-Eulerian  
448 problems. *Int. J. Numer. Methods Eng.* **92**, 857–890 (2012).

- 449 37. Jeunechamps, P.-P. & Ponthot, J.-P. An efficient 3D implicit approach for the  
450 thermomechanical simulation of elastic–viscoplastic materials submitted to  
451 high strain rate and damage. *Int. J. Numer. Methods Eng.* **94**, 920–960 (2013).
- 452 38. Mengoni, M. & Ponthot, J. P. A generic anisotropic continuum damage model  
453 integration scheme adaptable to both ductile damage and biological damage-like  
454 situations. *Int. J. Plast.* **66**, 46–70 (2015).
- 455 39. Mengoni, M. *et al.* A non-linear homogeneous model for bone-like materials under  
456 compressive load. *Int. J. Numer. Methods Biomed. Eng.* **28**, 273–287 (2012).
- 457 40. Helgason, B. *et al.* A modified method for assigning material properties to FE models  
458 of bones. *Med. Eng. Phys.* **30**, 444–453 (2008).
- 459 41. Taddei, F., Schileo, E., Helgason, B., Cristofolini, L. & Viceconti, M. The material  
460 mapping strategy influences the accuracy of CT-based finite element models of  
461 bones: an evaluation against experimental measurements. *Med. Eng. Phys.* **29**, 973–  
462 979 (2007).
- 463 42. Zeng, X., Wen, S., Li, M. & Xie, G. Estimating Young’s Modulus of Materials by a New  
464 Three-Point Bending Method. *Adv. Mater. Sci. Eng.* **2014**, e189423 (2014).
- 465 43. Doblaré, M., García, J. M. & Gómez, M. J. Modelling bone tissue fracture and healing:  
466 a review. *Eng. Fract. Mech.* **71**, 1809–1840 (2004).

- 467 44. Burkhart, T. A., Quenneville, C. E., Dunning, C. E. & Andrews, D. M. Development and  
468 validation of a distal radius finite element model to simulate impact loading  
469 indicative of a forward fall. *Proc. Inst. Mech. Eng. [H]* **228**, 258–271 (2014).
- 470 45. Peng, L., Bai, J., Zeng, X. & Zhou, Y. Comparison of isotropic and orthotropic material  
471 property assignments on femoral finite element models under two loading  
472 conditions. *Med. Eng. Phys.* **28**, 227–233 (2006).
- 473 46. Yang, H., Ma, X. & Guo, T. Some factors that affect the comparison between isotropic  
474 and orthotropic inhomogeneous finite element material models of femur. *Med. Eng.*  
475 *Phys.* **32**, 553–560 (2010).
- 476
- 477

478 **Figure captions**

479 Figure 1. Experimental and simulated bending test on canine humerus. (a) Preparation  
480 of bone samples using a custom jig to align resin moulds (b) bone samples embedded in  
481 resin moulds were mounted in a custom bending stand (c) the bending tests were  
482 simulated by simplifying the resin moulds with single hexahedrons linked to the bone  
483 surface (red dots) via artificial springs. A sticking contact condition was considered  
484 between the bending tool and the bone surface (green dots), while contact-friction  
485 interaction was considered between the resin moulds and the bending stand (blue  
486 cylinders).

487 Figure 2. Determined relation between canine bone properties as a function of mass  
488 based on existing data<sup>19</sup> and human bone properties.

489 Figure 3. Calculation of orthotropic axes (longitudinal and transverse for a transversely  
490 isotropic model) from the central third of the bone. Longitudinal direction is defined as  
491 the computed least-square line of the mesh nodes included in the bone diaphysis  
492 surface.

493 Figure 4: Left: bending responses of the fourteen humeri. Right: bending stiffness of the  
494 seven pairs of humeri, emphasizing the large inter- and intra-variability of measured  
495 responses.

496 Figure 5. Bone meshes resulting from the reconstruction of segmented CT images  
497 together with the mapping procedure. The colour code corresponds to the computed  
498 densities ( $\text{g}/\text{mm}^3$ ) assigned to each mesh element from HU values.

499 Figure 6. Left: experimental vs. simulated stiffness and yield load for the fourteen bone  
500 samples and for the density-dependent transversely isotropic model. The dash line  
501 represents a perfect prediction (simulation=experiments), whereas the continuous line  
502 represents the linear fitting of the data. Right: Prediction error on stiffness and yield  
503 load for the seven pairs of humeri.

504 Figure 7: Bland-Altman representation of the results obtained for the density-dependant  
505 transversely isotropic model in terms of bending stiffness (left) and yield load (right).  
506 Points are represented with the corresponding sample name (r=right, l=left).

507 Figure 8. Left: experimental vs. simulated stiffness and yield load for the fourteen bone  
508 samples and for both a density-dependent transversely isotropic model and a density-  
509 dependent isotropic model. Right: Prediction error on stiffness and yield load for these  
510 two models.

511 Figure 9. Left: experimental vs. simulated stiffness and yield load for the fourteen bone  
512 samples and for a two-material isotropic model. In this model, trabecular and cortical  
513 tissues are considered homogeneous and are separated from density thresholds of



514 400HU or 600HU issued the CT-scan. Right: Prediction error on stiffness and yield load  
515 for these two models.

516

517 **Table captions**

518 Table 1. Sensitivity analysis of the computational results : effect of resin properties,  
519 spring stiffness and friction coefficient between bending stand and resin on predicted  
520 bone stiffness and yield load. The star indicates a significant difference between a set of  
521 parameters and the selected parameters in the presented simulations.

522 Table 2. Confrontation of the computational and experimental results in terms of  
523 predicted yield load and bending stiffness. The p-value of ANOVA tests are given for  
524 density-dependent transversely isotropic models (trans. iso), density-dependant  
525 isotropic models (iso.) and two-materials isotropic models with segmentation threshold  
526 of 400HU (400HU) and 600HU (600 HU). Low p-values indicate a significant difference  
527 between experimental and simulation results.

528

Resin modulus (MPa)	Predicted Stiffness (N/mm)	Predicted yield load (N)	Spring stiffness (N/mm)	Predicted Stiffness (N/mm)	Predicted yield load (N)	Friction coefficient	Predicted Stiffness (N/mm)	Predicted yield load (N)
100	548.3	1500.2	1	532.3	1497.9	0.5	507.3	1425.9
500	548.3	1500.2	10	544.2	1500.1	0.6	527.2	1462.2
900	548.3	1500.2	100	548.8	1500.2	0.7	548.8	1500.2
1300	548.3	1500.2	1000	558.0	1489.4	0.8	572.2	1539.7
1700	548.3	1500.2	10000	544.0	1508.8	0.9	595.1	1590.8

529 Table 1 : Sensitivity analysis of the computational results : effect of resin properties, spring stiffness and  
530 friction coefficient on predicted bone stiffness and yield load.

531

532

533

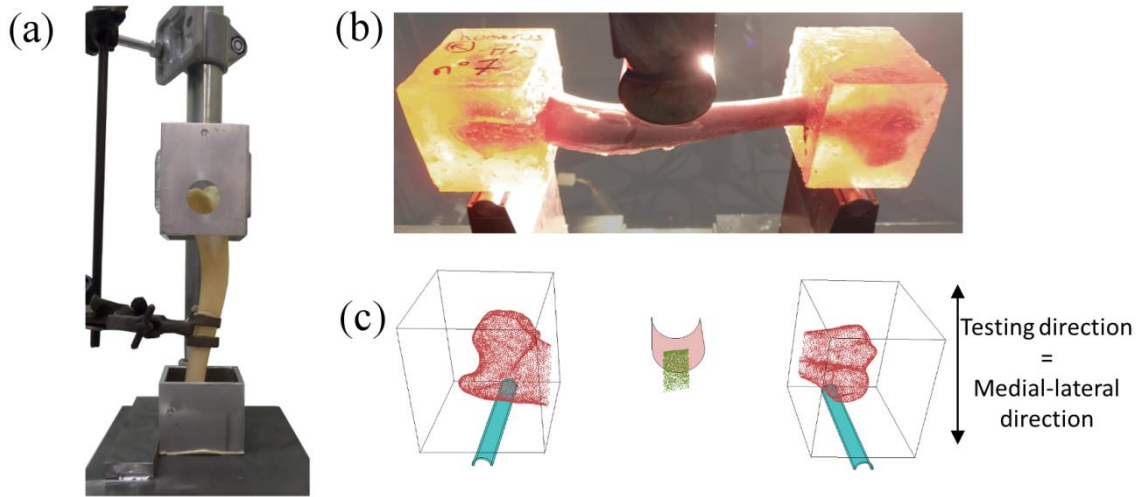
	Stiffness (N/mm)				Yield load (N)			
	Trans. Iso.	Iso.	400HU	600HU	Trans. Iso.	Iso.	400HU	600HU
<i>p-value</i> of the ANOVA test	0,67	2.48 10 <sup>-4</sup>	0,43	0,17	0,74	4.13 10 <sup>-5</sup>	0,18	0,08

534

535 Table 2: Confrontation of the computational and experimental results in terms of predicted yield load  
536 and bending stiffness. The *p-value* of ANOVA tests are given for density-dependent transversely  
537 isotropic models (trans. iso.), density-dependant isotropic models (iso.) and two-materials isotropic  
538 models with segmentation threshold of 400HU (400HU) and 600HU (600 HU). Low *p-values* indicate a  
539 significant difference between experimental and simulation results.

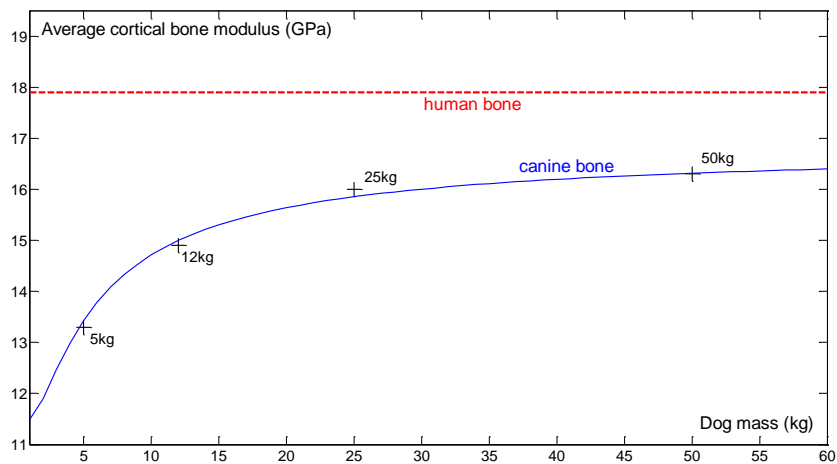
540

541



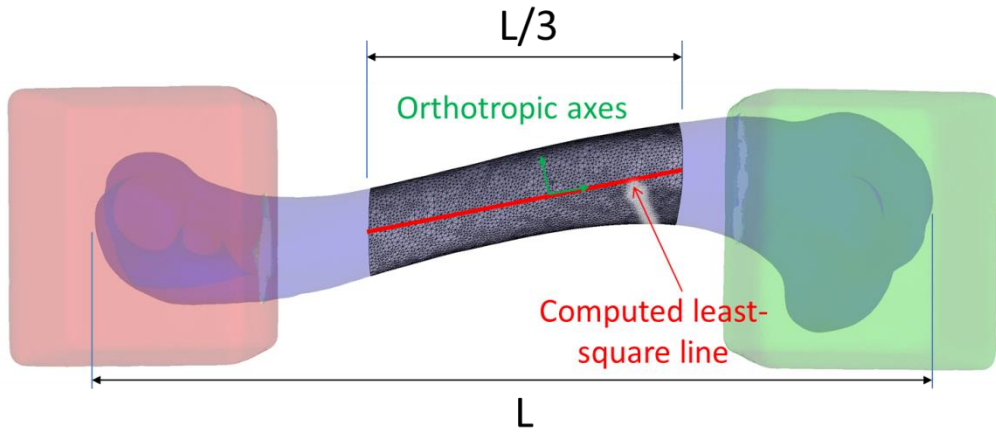
542  
543  
544  
545  
546  
547  
548  
549

Figure 1: Experimental and simulated bending test on canine humerus. (a) Preparation of bone samples using a custom jig to align resin moulds (b) bone samples embedded in resin moulds were mounted in a custom bending stand (c) the bending tests were simulated by simplifying the resin moulds with single hexahedrons linked to the bone surface (red dots) via artificial springs. A sticking contact condition was considered between the bending tool and the bone surface (green dots), while contact-friction interaction was considered between the resin moulds and the bending stand (blue cylinders).



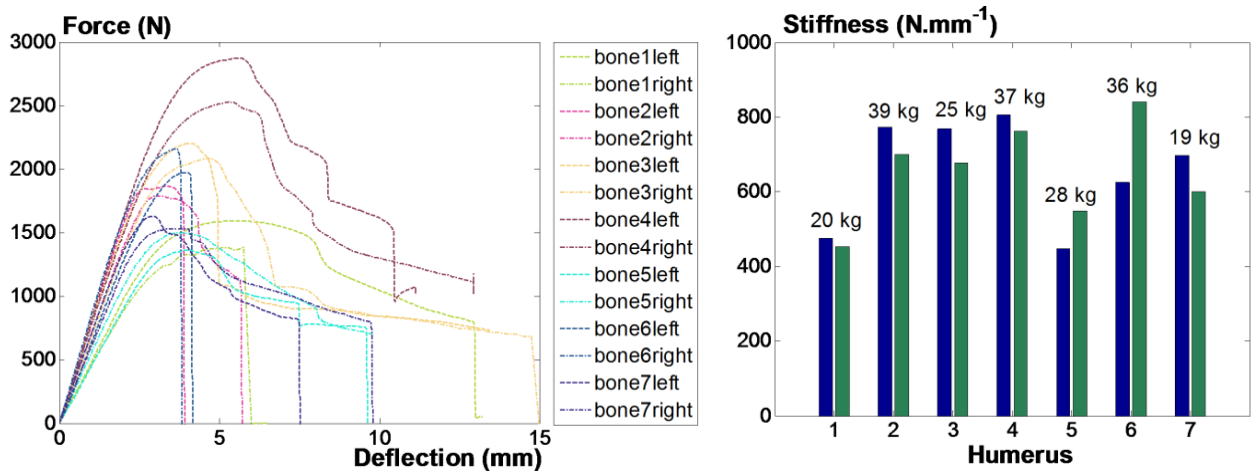
550  
551  
552  
553

Figure 2. Determined relation between canine bone properties as a function of mass based on existing data<sup>19</sup> and human bone properties.



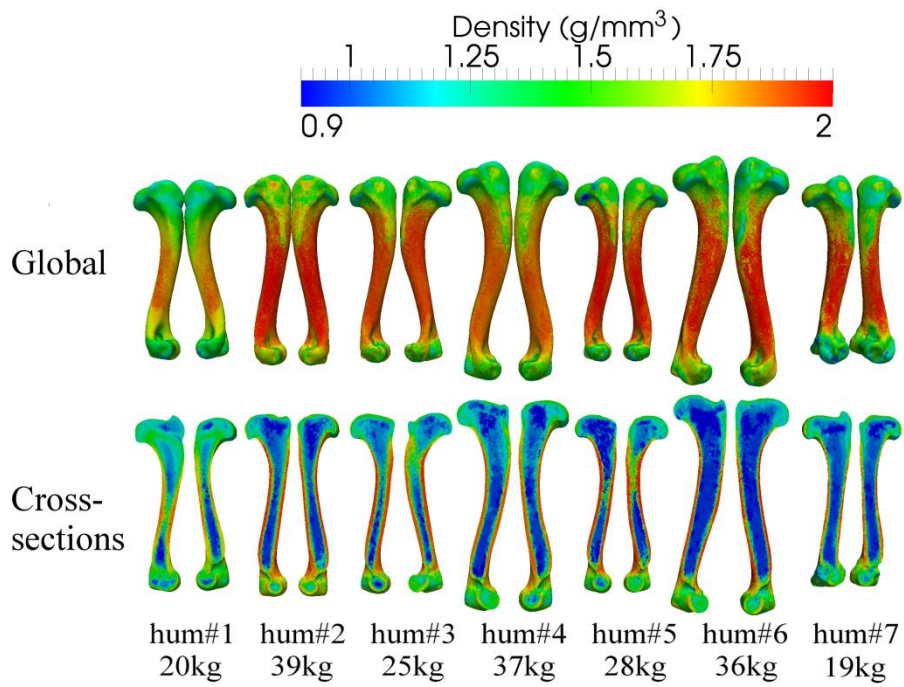
554  
 555  
 556  
 557  
 558  
 559

Figure 3. Calculation of orthotropic axes (longitudinal and transverse for a transversely isotropic model) from the central third of the bone. Longitudinal direction is defined as the computed least-square line of the mesh nodes included in the bone diaphysis surface.



560  
 561  
 562

Figure 4: Left: bending responses of the fourteen humeri. Right: bending stiffness of the seven pairs of humeri, emphasizing the large inter- and intra-variability of measured responses.



563

564

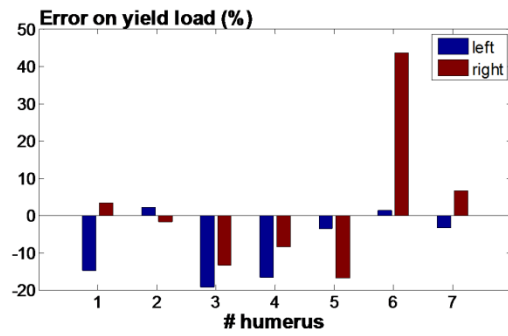
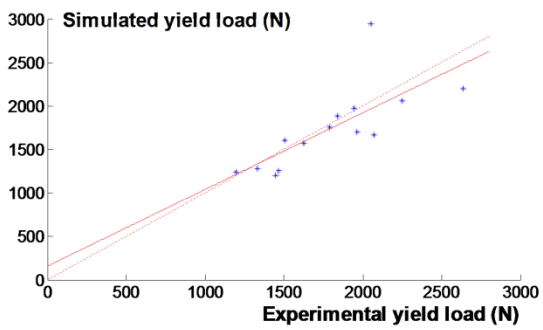
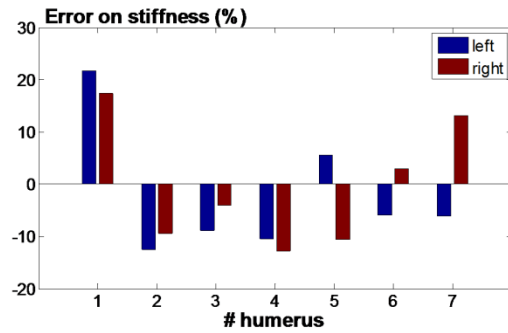
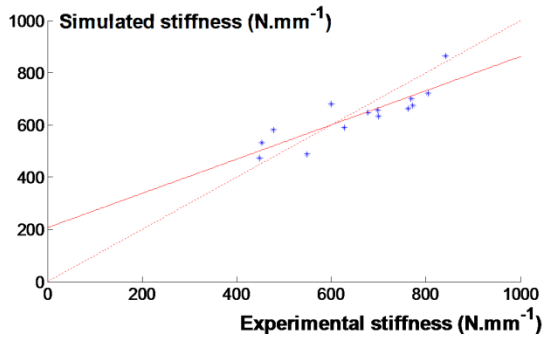
565

566

567

568

Figure 5. Bone meshes resulting from the reconstruction of segmented CT images together with the mapping procedure. The colour code corresponds to the computed densities (g/mm<sup>3</sup>) assigned to each mesh element from HU values.



569

570

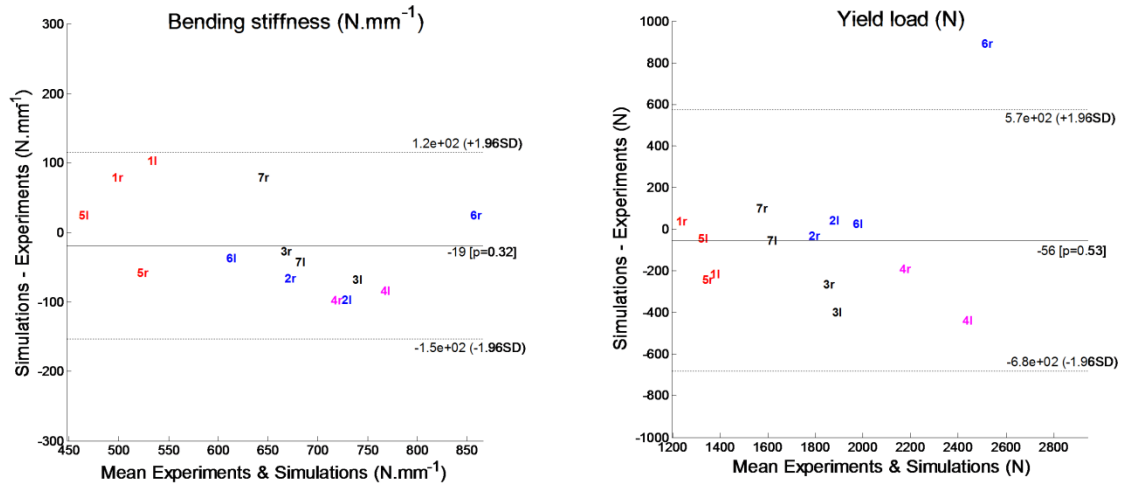
571

572

573

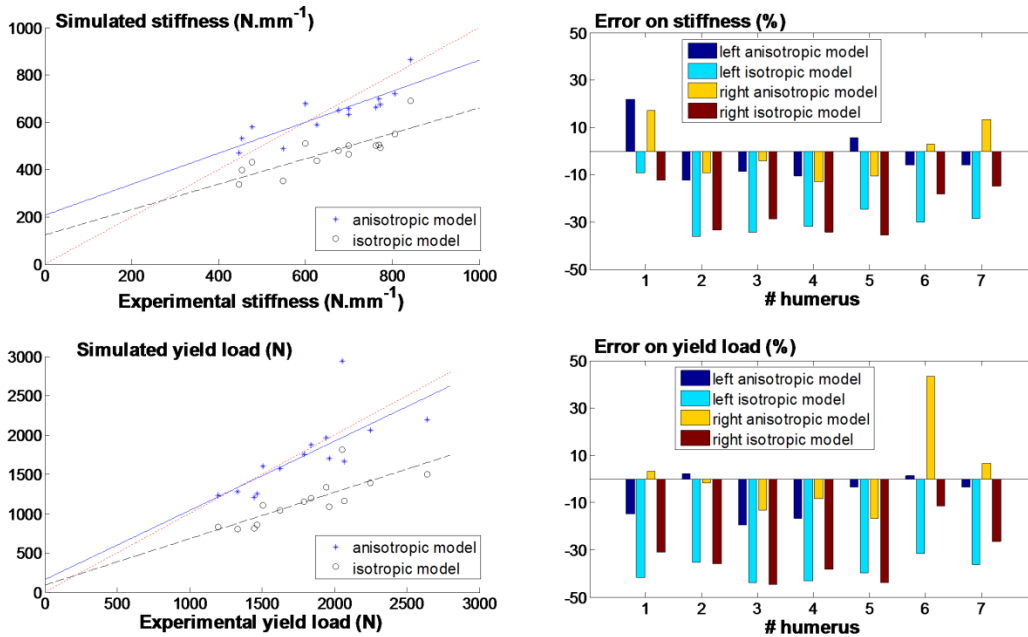
574

Figure 6. Left: experimental vs. simulated stiffness and yield load for the fourteen bone samples and for the density-dependent transversely isotropic model. The dash line represents a perfect prediction (simulation=experiments), whereas the continuous line represents the linear fitting of the data. Right: Prediction error on stiffness and yield load for the seven pairs of humeri.



575  
576  
577  
578

Figure 7 : Bland-Altman representation of the results obtained for the density-dependant transversely isotropic model in terms of bending stiffness (left) and yield load (right). Points are represented with the corresponding sample name (r=right, l=left).



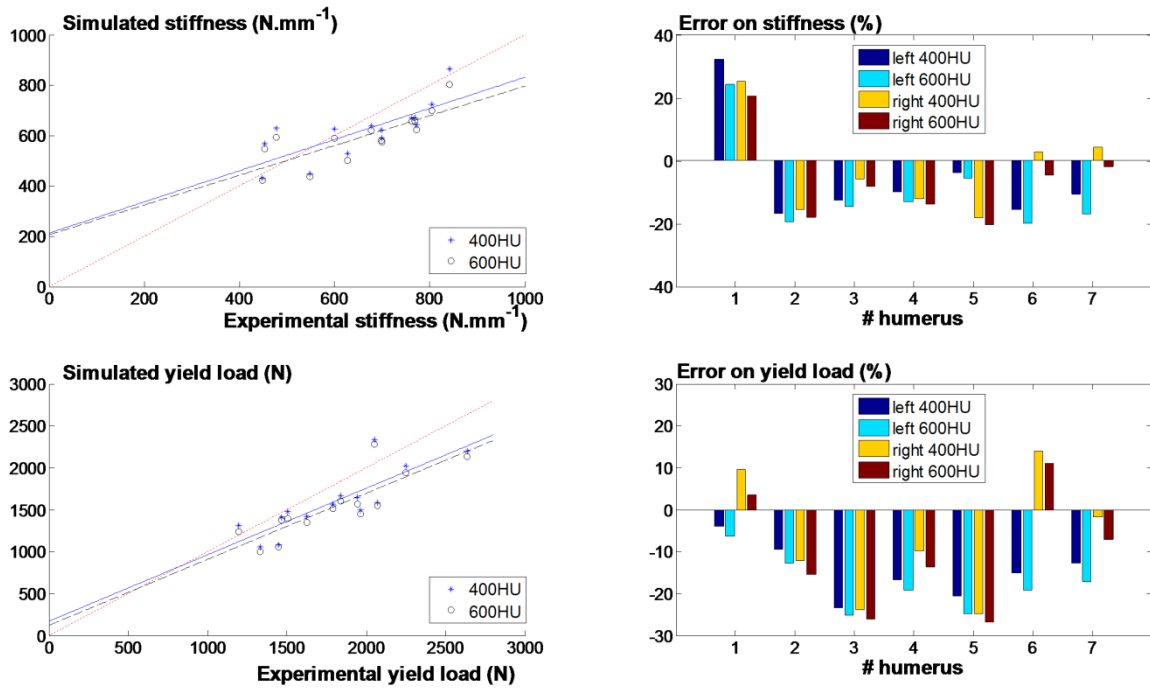
579  
580  
581  
582  
583

Figure 8. Left: experimental vs. simulated stiffness and yield load for the fourteen bone samples and for both a density-dependent transversely isotropic model and a density-dependent isotropic model. The red dash line represents a perfect prediction (simulation=experiments). Right: Prediction error on stiffness and yield load for these two models.



584

585



586

587

588

589

590

591

592

Figure 9. Left: experimental vs. simulated stiffness and yield load for the fourteen bone samples and for a two-material isotropic model. In this model, trabecular and cortical tissues are considered homogeneous and are separated from density thresholds of 400HU or 600HU issued the CT-scan. The red dash line represents a perfect prediction (simulation=experiments). Right: Prediction error on stiffness and yield load for these two models.